JGR Space Physics

TECHNICAL REPORTS: DATA

10.1029/2019JA027729

Fine-Scale Visualization of Aurora in a Wide Area Using Color Digital Camera Images From the International Space Station

Sota Nanjo[1], Yuta Hozumi[1], Keisuke Hosokawa[1], Ryuho Kataoka[2,3], Yoshizumi Miyoshi[4], Shin-ichiro Oyama[2,4,5], Mitsunori Ozaki[6], Kazuo Shiokawa[4], and Satoshi Kurita[4]

[1]Graduate School of Communication Engineering and Informatics, The University of Electro-Communications, Chofu, Japan, [2]National Institute of Polar Research, Tachikawa, Japan, [3]Department of Polar Science, School of Multidisciplinary Sciences, SOKENDAI, The Graduate University for Advanced Studies, Tachikawa, Japan, [4]Institute for Space-Earth Environmental Research, Nagoya University, Nagoya, Japan, [5]Ionospheric Physics Research Unit, University of Oulu, Oulu, Finland, [6]Graduate School of Natural Science and Technology, Kanazawa University, Kanazawa, Japan

Key Points:
- Accurate mapping method of the photographs taken from ISS was established
- Mapped ISS images can be used for the study of fast moving aurora
- Unique wide FOV auroral data will reveal some global spatiotemporal variations of pulsating aurora

Supporting Information:
- Supporting Information S1
- Movie S1
- Movie S2

Correspondence to:
S. Nanjo,
sota.nanjo@uec.ac.jp

Citation:
Nanjo, S., Hozumi, Y., Hosokawa, K., Kataoka, R., Miyoshi, Y., & Oyama, S.-i. (2020). Fine-scale visualization of aurora in a wide area using color digital camera images from the International Space Station. *Journal of Geophysical Research: Space Physics*, *125*, e2019JA027729. https://doi.org/10.1029/2019JA027729

Received 12 DEC 2019
Accepted 21 FEB 2020
Accepted article online 22 FEB 2020

Abstract The full-color photographs of aurora have been taken with digital single-lens reflex cameras mounted on the International Space Station (ISS). Since these photographs do not have accurate time and geographical information, in order to use them as scientific data, it is necessary to calibrate the imaging parameters (such as looking direction and angle of view of the camera) of the photographs. For this purpose, we calibrated the imaging parameters using a city light image taken from the Defense Meteorological Satellite Program satellite following the method of Hozumi et al. (2016, https://doi.org/10.1186/s40623-016-0532-z). We mapped the photographs onto the geographic coordinate system using the calibrated imaging parameters. To evaluate the accuracy of the mapping, we compared the aurora taken simultaneously from ISS and ground. Comparing the spatial structure of discrete aurora and the temporal variation of pulsating aurora, the accuracy of the data set is less than 0.3 s in time and less than 5 km in space in the direction perpendicular to the looking direction of the camera. The generated data set has a wide field of view (~1,100 × 900 km), and their temporal resolution is less than 1 s. Not only that, the field of view can sweep a wide area (~3,000 km in longitude) in a short time (~10 min). Thus, this new imaging capability will enable us to capture the evolution of fine-scale spatial structure of aurora in a wide area.

1. Introduction

Aurorae are luminous and colorful phenomena seen in the high-latitude part of the Earth's upper atmosphere at altitudes from 90 to 300 km (Jones, 1971). Such auroral emissions originate from atoms and molecules excited by energetic charged particles precipitating from the magnetosphere along the Earth's magnetic field line. This allows us to employ the two-dimensional distribution of optical emission as a proxy for the pattern of particles precipitating from the magnetosphere (e.g., Akasofu, 1965). In this sense, optical observations of aurora are of particular importance in monitoring the Geospace environment on the Earth's atmosphere in the framework of space weather forecasting.

For such purposes, various types of optical observations have been performed in the history. Especially, ground-based optical observations have been carried out since 1960s. In the early stage of ground-based observations, the images are recorded at the video rate (30 Hz) (e.g., Davis, 1966; Scourfield & Parsons, 1969). Recently, the Electron Multiplying Charge Coupled Device (EMCCD) all-sky imagers (ASIs) are used to obtain images with further improved temporal resolution such as 0.01 s (i.e., 100 Hz sampling) (e.g., Nishiyama et al., 2012; Ozaki et al., 2016). Those high temporal resolution optical measurements are fairly sufficient to track fast modulations in aurora (e.g., pulsating aurora: PsA) (e.g., Hosokawa et al., 2015; Lessard, 2012). However, a single ASI has a limitation in the coverage of the field of view (FOV). In order to overcome this problem, the Time History of Events and Macroscale Interactions during Substorms ground-based observation (THEMIS-GBO) succeeded in imaging the detailed spatial structure of aurora in a wide area extending from Alaska to Labrador by deploying a cluster of ASIs as a network (Mende et al., 2008).

However, the temporal resolution of the THEMIS-GBO imagers is 3 s, which is often insufficient for detecting the rapid temporal variation of PsA. Moreover, since the ground-based observation is greatly affected by the local weather conditions, the probability of the simultaneous observations at multiple stations is not high. For these reasons, wide FOV optical observations from space have been highly demanded.

Since the late 1970s, optical instruments onboard satellites such as Freja (Marklund et al., 1998), Viking (Elphinstone et al., 1995), DE-2 (Killeen et al., 1988), Akebono (Oguti et al., 1990), and Polar (Acuña et al., 1995) have visualized large-scale structures of aurora from space. In the 2000s, several ultraviolet (UV) cameras having a wide FOV onboard the IMAGE satellite (Burch, 2000) have widely been used for studies of aurora (e.g., Burch et al., 2001). In particular, a lot of researchers have investigated the relationship between the temporal evolution of the entire auroral oval and the solar wind parameters (e.g., Milan et al., 2009; Zhang et al., 2002). However, because of the use of low spatial resolution (~52 km × 52 km, Mende et al., 2000) UV imaging, it has been difficult to image the fine-scale structure of aurora such as typical patches of PsA whose spatial scale ranges from a few tens to a few hundreds of kilometer. After that, the multispectral auroral camera (MAC) instrument (Sakanoi et al., 2003) onboard the Reimei satellite succeeded in observing the fine-scale structure of discrete aurora (Asamura et al., 2009) and the rapid temporal variation of PsA (Miyoshi et al., 2015) using visible lights. Still, however, the limited FOV of MAC (~80 km × 80 km, Sakanoi et al., 2003) did not allow us to observe such fine-scale/fast variations of aurora in a wide area. Thus, it is still difficult to observe the detailed spatial/temporal characteristics of aurora in a wide area, which has been a major obstacle for revealing the origin of the fine structure and the rapid temporal variation of aurora.

To overcome this limitation, we use the color digital camera photographs from the International Space Station (ISS) for the study of aurora. The color photographs (ISS photographs) taken in the rim of the Earth direction often have spatial and temporal resolutions sufficient for studying aurora, and those photographs are available online with Photo ID (Gateway to Astronaut Photography of Earth, 1995). However, they do not have accurate time and geographical information because they have not been taken for the purpose of scientific researches. If we correctly estimate the so-called imaging parameters (such as looking direction and angle of view of the camera) by calibrating the photographs, we could project the color photographs onto the altitude of auroral emission with accurate time stamps, which would be utilized for researches of various kinds of aurora. Riechert et al. (2016) proposed a calibration method of the photographs using star lights, but it was not possible to guarantee the time accuracy because the change of the apparent positions of star lights is small relative to the demanded time resolution of 1 s or less. They argued that additional use of city light positions can reduce the error in time to 1 s. However, since they did not take the distortion of window into consideration, the geographical location of the projected points has errors larger than 20 km.

Later, Hozumi et al. (2016) proposed another calibration method of the ISS photographs using city lights in the images. Since city lights are located much closer to the camera onboard the ISS than star lights, rapid change of their apparent positions in time enables us to better estimate the imaging parameters. They used a city light image captured by the Operational Linescan System (OLS) sensor of the Defense Meteorological Satellite Program (DMSP) satellite (Version 4 DMSP-OLS Nighttime Lights Time Series, 2015) as a reference for the city light location. They employed the calibrated photographs for the studying airglow in the low-latitude region and proved the accuracy of the proposed method by comparing the height profile of the derived emission with the location of equatorial anomaly. In this study, we applied the method of Hozumi et al. (2016) for mapping discrete aurora and PsA and examined the feasibility of using the photographs for the research of aurora at high latitudes. In particular, through comparison between the mapped ISS photographs and simultaneously obtained ground-based ASI observations, we clarify (1) whether we are able to map the spatial structure of discrete aurora correctly and (2) whether we are able to extract the temporal variation of PsA.

2. Data Set and Method

2.1. Data Set

ISS has been orbiting the Earth with a period of ~90 min with an inclination angle of 51.6°. The orbital altitude of ISS is about 400 km, from which the digital camera observations have often been performed in the rim of the Earth direction (mostly looking north at high latitudes). During the events focused in this paper, Nikon D4 was used for a digital single-lens reflex camera and AF-S NIKKOR 24 mm f/1.4G ED was used for the lens. The size of the photographs taken by the camera was 4,928 × 3,280 pixels, and the temporal resolution was 1 s. The exposure time of the image capturing was 1/3 s, and the ISO speed rate was 5,000.

The data from the THEMIS-GBO ASI (THEMIS ASI) installed in Gakona, Alaska (62.41° N, 145.16° W) and the EMCCD ASI installed in Athabasca, Canada (54.60° N, 113.64° W) were used for the comparisons with the mapped ISS photographs. The THEMIS ASI observes all visible light (i.e., panchromatic observation) with a temporal resolution of 3 s. The EMCCD ASI has a temporal resolution of 0.01 s and observes only the prompt emission by using the BG3 filter (Samara et al., 2012), which allows us to filter out typical green aurora (5,577 Å). Hereinafter, a rim direction photograph taken from the ISS is called "ISS image," a city light image captured by the OLS sensor of the DMSP satellite is called "DMSP image," and an image taken by ground-based ASI is called "ASI image."

2.2. Methods

Hozumi et al. (2016) have proposed a calibration method for the ISS images using city lights. The detailed method is as follows. By applying the pinhole camera model (e.g., Jähne, 1997; Trucco & Verri, 1998), the relation between a city light position on the Earth and that in the ISS image is given by the following equations:

$$\begin{bmatrix} x \\ y \\ z \end{bmatrix} = R \begin{bmatrix} X \\ Y \\ Z \end{bmatrix} - t, \tag{1}$$

$$u = f\frac{x}{z} + C_x, \tag{2}$$

$$v = -f\frac{y}{z} + C_y, \tag{3}$$

where $[x \quad y \quad z]^T$ is the position of the city light in the camera coordinate system fixed to the camera on ISS and $[X \quad Y \quad Z]^T$ is the position of the city lights in the world coordinate system. In equation (1), t is the camera position in the world coordinate system, and R is the rotation matrix representing the looking direction of the camera. The matrix R transforms a point in the world coordinate system to the camera coordinate system. In equations (2) and (3), (u, v) is the coordinate of the city lights in the DMSP image projected onto the ISS image, and the focal length f is a function of the angle of view (AOV) as expressed by $f = \frac{1}{\tan(\mathrm{AOV}/2)}\frac{N_{\mathrm{pix}}}{2}$, where N_{pix} is the number of horizontal pixels of the ISS image. (C_x, C_y) is the position of the center of the ISS image in units of pixel. The Euler angles θ, σ, and ϕ are used to describe the looking direction of the camera relative to ISS. The relation between R and the ISS orientation R_{ISS} can be expressed as a function of the Euler angles:

$$R = \begin{bmatrix} \cos\phi & \sin\phi & 0 \\ -\sin\phi & \cos\phi & 0 \\ 0 & 0 & 1 \end{bmatrix} \begin{bmatrix} \cos\sigma & 0 & -\sin\sigma \\ 0 & 1 & 0 \\ \sin\sigma & 0 & \cos\sigma \end{bmatrix} \begin{bmatrix} 1 & 0 & 0 \\ 0 & \cos\theta & \sin\theta \\ 0 & -\sin\theta & \cos\theta \end{bmatrix} R_{\mathrm{ISS}}. \tag{4}$$

In order to remove the lens distortion, the following equations were used according to Brown's (1971) lens distortion model:

$$u_{\mathrm{correct}} = u(1 + k_1 r^2 + k_2 r^4), \tag{5}$$

$$v_{\mathrm{correct}} = v(1 + k_1 r^2 + k_2 r^4), \tag{6}$$

where r is the distance from the center of the ISS image in units of pixel and k_1 and k_2 are the radial distortion coefficients. Using the above equations, we can project the city lights in the DMSP image onto the ISS image.

During the imaging sequence, the camera location was assumed to be the same as that of ISS. Although the location of ISS is given as a function of time, the time stamp recorded in the metadata of the ISS image is not accurate because it is not routinely adjusted with a reliable time server such as GPS. Therefore, it is also necessary to treat the time stamp as an unknown parameter. Since the attitude of ISS is also given as a function of time, the looking direction of the ISS camera can also be determined if the time lag is estimated correctly. Regarding the estimation of the time of the ISS image, we interpolated the ISS position provided every 1 s with 0.1 s intervals using the spline function. Eventually, we need to determine the seven unknown parameters (three Euler angles, time lag, AOV, and two distortion coefficients k_1 and k_2). Once a parameter set is assumed, a virtual view city light image is created from the DMSP image using equations (1)–(6). To find the best parameter set, the mean distance between the city light positions in the ISS image and those in a virtual image is calculated. This process keeps iterated over the parameter space until the mean distance reaches a minimum value. There are seven unknown parameters in total, and each city light has

two-dimensional information; thus, it is sufficient to use at least four city lights for the calibration process. However, in order to further improve the accuracy, we use more than four city lights. The city lights used for the calibration have to be selected manually, but as small as possible ones were chosen intensionally from a wide area to improve accuracy. In addition, to evaluate the variance of the parameters, we carry out the calibration with several ISS images taken during a single sequence of the photographs. Note that each ISS image contains a different set of city lights, so the combinations of city lights used for the calibration were different for each case. Since the position and orientation of ISS are given as a function of time, it is sufficient to use only single parameter set throughout the sequence. Therefore, a parameter set that minimized the mean distance was used for mapping all the photographs in the sequence.

Once the seven imaging parameters are determined, each pixel of the ISS image can be projected onto the surface of the emission altitude of aurora at 110 km by the following procedure. First, we consider a line-of-sight vector of each pixel of the ISS image and a WGS84 spheroid whose major and minor axes radius are R_E+ 110 km. Then the intersection points of the spheroid and the line-of-sight vector are calculated. In actual, two intersection points are derived, but we choose the one closer to ISS because it is the desired point of projection. We can map the entire ISS image onto the altitude of aurora in the geographic coordinate system by carrying out the above calculation for all the pixels. However, in order to reduce the resource for computation, we prepare latitude/longitude grids having 0.05° resolution and only calculate the pixels corresponding the vertexes of these grids. It is necessary to assume the projection altitude in each case, but we followed previous researches (e.g., Brown et al., 1976; Kataoka et al., 2013; Romick & Belon, 1967), and it was assumed to be 110 km for discrete aurora and 100 km for PsA.

In order to evaluate the validity of the proposed mapping method, we compared the spatial/temporal variations of discrete aurora and PsA seen in the ISS images with those simultaneously captured by the ground-based ASIs. Since the ISS images are full color, it is preferable to use the THEMIS ASI which observes all the visible lights for comparison. For PsA, however, it is needed to use the EMCCD ASI because the temporal resolution of the THEMIS ASI (3 s) is close to the typical pulsating period of PsA. When comparing, the EMCCD ASI data were down-sampled to ∼3 Hz to match the exposure time of the ISS image. In addition, to evaluate the time accuracy of the ISS image, we performed a cross-correlation analysis of the two time series of optical intensity (i.e., ISS image and ground-based ASI image) with a 0.1 s resolution of shifted time. The ISS camera has three channels (i.e., red, green, and blue), and it might be preferable to use the green channel to observe the typical green aurora (5,577 Å). However, the EMCCD ASI observes prompt emission of N_2^+ and N_2 (e.g., 4,278 Å; 8,446 Å); thus, the blue channel was used for the comparisons instead of the green one.

3. Results

3.1. Calibration Result

We calibrated the imaging parameters for several photographs in the sequence obtained on 28 September 2017. During this image sequence from 07:38 to 07:55 UT, ISS was on a pass from the northern Pacific Ocean, just south of Alaska, down to the Gulf of Mexico, south of Florida (the approximate trajectory and image sequence are available at https://eol.jsc.nasa.gov/SearchPhotos/ShowQueryResults-TextTable.pl?results=1573195985157562). The aurora was observed above Alaska and central Canada from 07:38 to 07:47 UT. An example of the rim direction ISS images used for the calibration is shown in Figure 1a, where the locations of the eight city lights used for the calibration process are marked by the blue circles. At this time, ISS was located near Seattle (48.32° N, 121.31° W), and the camera was pointing toward the northeastward direction and looking at a broad region of diffuse aurora distributing in the northern Canada. Figure 1b provides the reference city light image from DMSP satellite covering the corresponding area, in which the eight city lights indicated in Figure 1a are again marked by the red circles.

We calibrated the imaging parameters for five ISS images in this sequence. When the imaging parameters were calibrated by comparing these two images, the resolution of time lag was set to 0.1 s, those of angles were 0.01° , and those of k_1 and k_2 were 10^{-11} and 10^{-18}, respectively. Table 1 is a summary of the calibration results. The top row of Table 1 is the best parameter set, and the bottom row provides the standard deviation of each parameter. It can be seen that each parameter does not change with time. This result suggests the validity of using single parameter set for the entire sequence. The fake shot made from the DMSP image with the best parameter set is given in Figure 1c, which demonstrates that the best parameter set reproduces exactly the same viewing geometry as that of the ISS image shown in Figure 1a. In Figure 1d, we overplotted

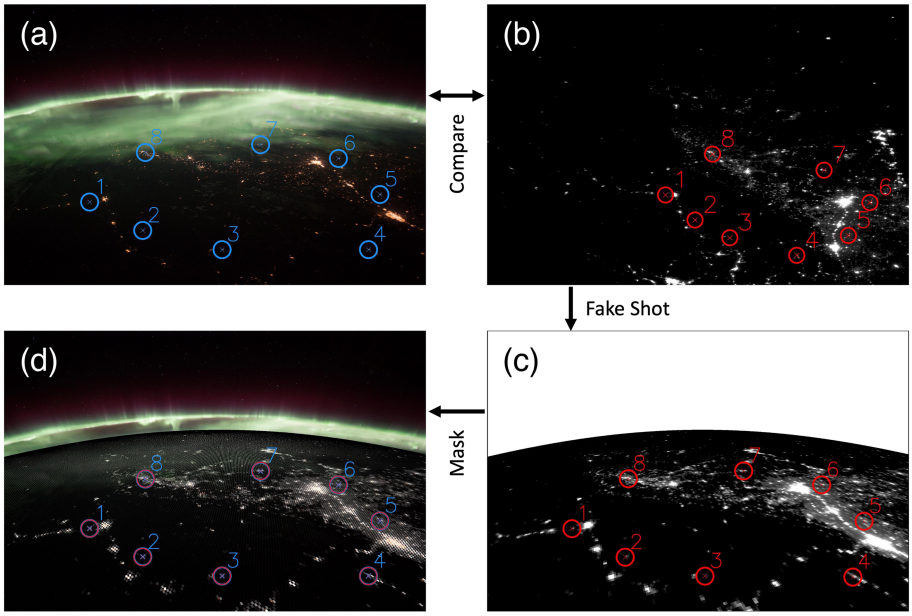

Figure 1. The calibration flow of a rim direction photograph taken from ISS using city light image taken from the DMSP satellite: (a) Photograph taken from ISS at 07:44:23 UT on 28 September 2017. Recorded Photo ID is ISS053-E-51088. The city lights enclosed by the blue circle were used for the calibration. (b) City light image taken from the DMSP satellite in the corresponding area captured from ISS. (c) Virtual view image obtained by processing (b) using an assumed parameter set (we have used the best parameter set for this case). (d) Image of (b) overlaid on (a). We have calculated the mean distance between the city lights enclosed by the blue and red circles and estimated the best parameter set.

the fake shot DMSP image onto the original ISS image, which again confirms the accuracy of the mapping result. The best parameter set, giving a minimum mean distance of 2.2 pixels, was employed for mapping all ISS images during the sequence. In the first half of this sequence on 28 September 2017, we saw a few discrete aurorae over the southern Alaska, and later, when the FOV of the ISS camera covered the northern Canada, clear signatures of PsA were captured. In the subsequent sections, we compare the mapped ISS images of discrete aurora and PsA with those simultaneously obtained from the ground-based ASIs having a common FOV with the mapped ISS images.

3.2. Mapping Result: Discrete Aurora

First, we mapped the discrete aurora arcs in the beginning of the interval using the estimated "best parameter set" described in Table 1. The arcs were observed in the southern Alaska by both the ISS camera and the THEMIS ASI in Gakona, Alaska. The snapshot images from both the optical instruments every 18 s are shown in Figure 2 which have already mapped onto the geographic coordinate system. An animation showing the full sequence of those images accompanies the electronic version of this article (Movie S1). The colored images are from ISS, and monochromatic images are from the ground-based ASI. To map the ground-based ASI images on the geographic coordinate system, we have assumed the emission height of 110 km and ignore the pixels whose elevation angle is less than 20° . Note that the black area in the upper

Table 1
Imaging Parameters Determined by the Calibration

Photo ID	Recorded time (UT)	# of city lights	Time lag (s)	θ (deg)	σ (deg)	ϕ (deg)	AOV (deg)	$k_1(\times 10^{-9})$	$k_2(\times 10^{-16})$
51088	7:44:23	8	−5.6	−86.41	−118.49	−86.17	72.50	−1.4	−1.4
51036	7:43:31	8	−5.1	−86.05	−118.45	−86.04	72.38	−2.3	−1.7
51060	7:43:55	8	−5.4	−86.28	−118.48	−86.08	72.17	−6.1	6.2
51380	7:49:15	8	−5.4	−84.34	−118.67	−83.81	72.58	−2.2	1.8
51550	7:52:05	7	−5.8	−84.14	−118.74	−83.48	72.75	2.8	−9.8
SD			0.3	1.11	0.13	1.35	0.22	3.2	5.9

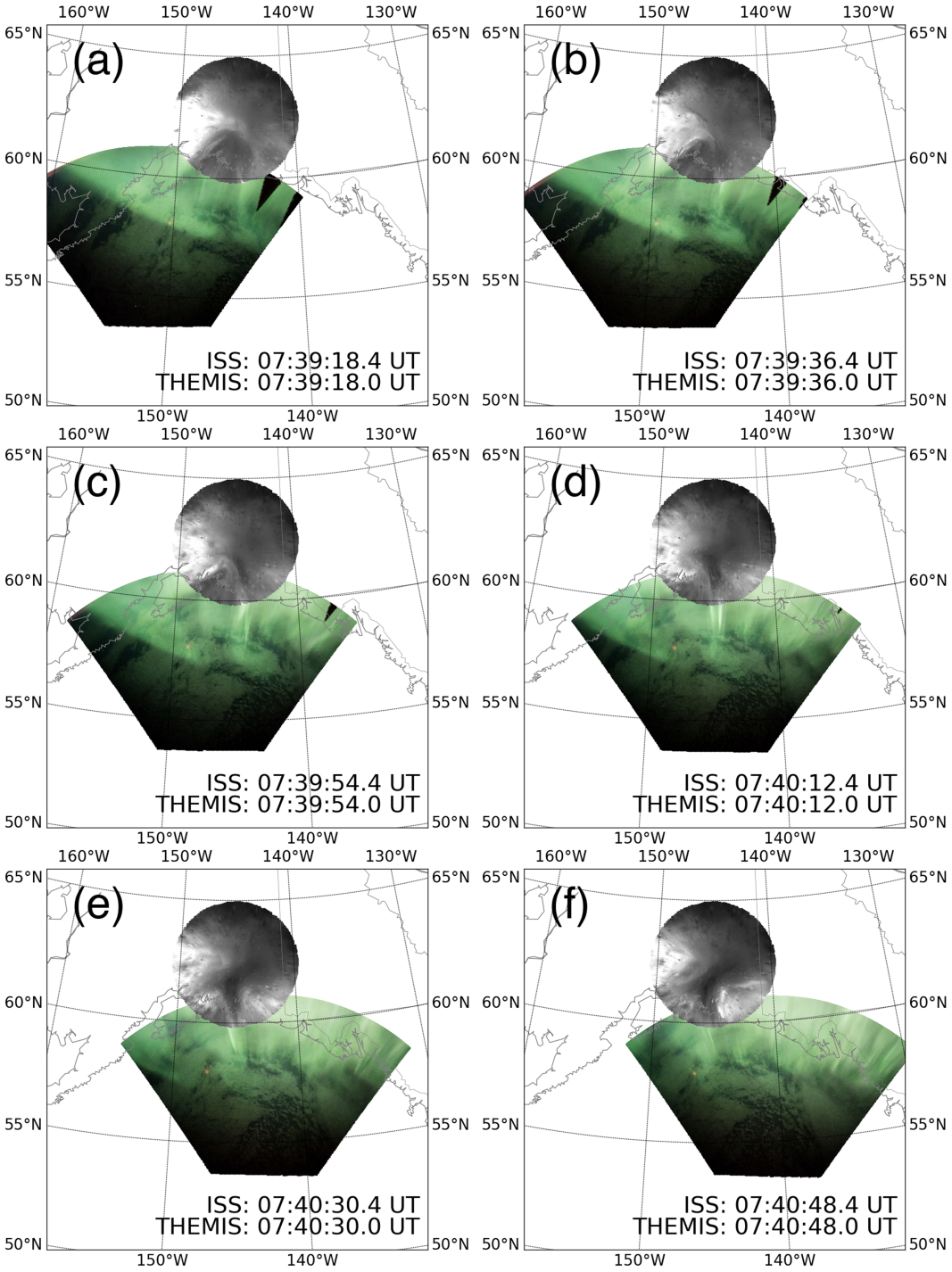

Figure 2. Snapshots of discrete aurora in the southern Alaska observed from both of the ISS camera and THEMIS ASI at Gakona, during 07:39–07:41 UT on 28 September 2017. The observed images were mapped onto the geographical coordinates by assuming that the aurora emission was at an altitude of 110 km.

right part of the ISS images is the solar panel of ISS and the mottled patterns seen in the ASI images are water droplets on the optical dome or cloud. Although there was 0.4 s offset in the timing of image capturing between the ISS camera and the THEMIS ASI due to the coarse cadence of the ASI, the approximate shape of the discrete aurora features in both the images is almost consistent throughout the sequence. However, there are a few mismatches between the observations from space and from ground, which will be discussed in the next part.

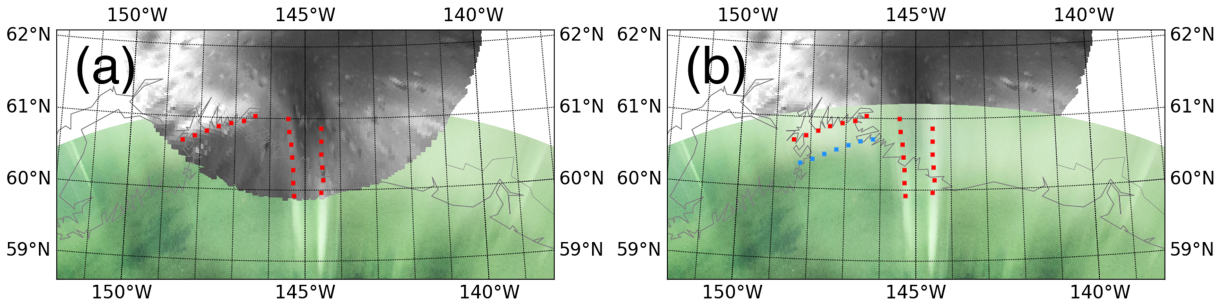

Figure 3. (a) Zoom-in images of Figure 2d. The red dashed lines trace discrete aurora observed by the THEMIS ASI. (b) Same data as (a), but the ISS image is overplotted on the THEMIS ASI image. The red dashed lines in (a) are again plotted. The blue horizontal dashed line indicates the shape of discrete aurora observed only by the ISS camera.

Figure 3 gives a zoom-in view of Figure 2d where two discrete arcs extending from north to south (so-called N-S arc) were seen in the intersection region of FOVs of the ISS camera and ASI. Such characteristic N-S arcs are traced by the vertical red dashed lines in Figure 3a. Figure 3b displays the same data as Figure 3a, but, in this case, the ISS image is overplotted on the ground-based ASI image to better show the consistent location of the N-S arcs in both the data. The red dashed lines marking the location of N-S arcs in the THEMIS ASI image well trace the similar N-S structure in the ISS image. That is, the two N-S arcs parallel to the line of sight of the ISS camera are seen in the same geographic location in both the image within an offset of 0.1° (~5 km) in the longitudinal direction.

In contrast to the two N-S arcs, the blue dashed line in Figure 3b outlines another clear discrete arc captured by the ISS camera, elongating more in the east to west direction. This arc was not observed by the THEMIS ASI in the same geographic location but was located slightly poleward as indicated by the horizontal dashed red line in Figure 3a. Namely, the structure perpendicular to the line of sight of the ISS camera has a spatial offset between the two images, which was about 0.3° (~30 km) in the latitudinal direction. Thus, the accuracy in the mapping of ISS images depends on the relationship between the direction of discrete arc elongation and the line of sight of the ISS camera, which will be discussed in detail in section 4.

3.3. Mapping Result: Pulsating Aurora

Here we introduce the mapping results for a case of PsA seen in the later interval during the same image sequence, when ISS flew over the central Canada. At around 07:45 UT, the PsA feature was observed by both the ISS camera and the EMCCD ASI in Athabasca, Canada. The FOV of the EMCCD ASI was embedded well within the viewing area of the ISS camera. Figure 4 highlights the result of the comparison between the two

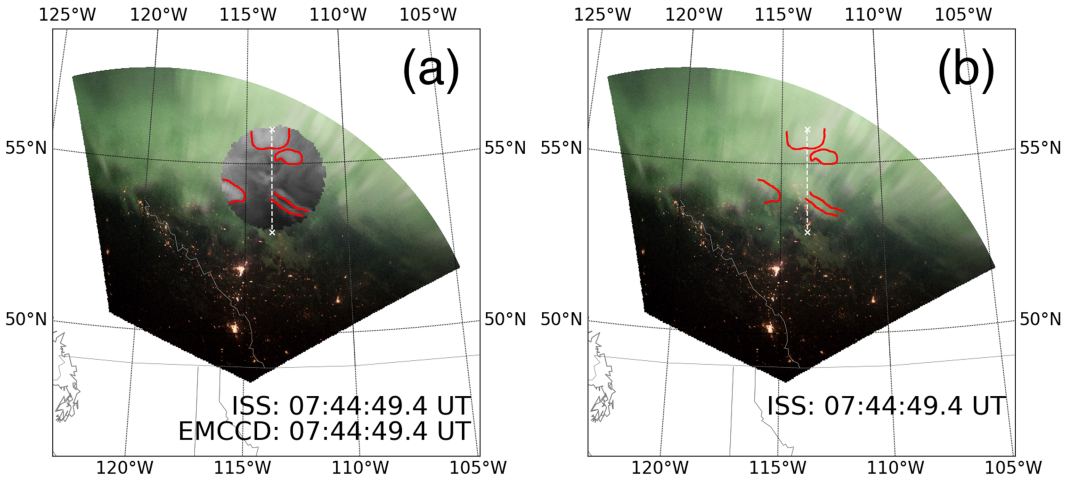

Figure 4. PsA observed by both the EMCCD ASI and the ISS camera, at 07:44:49.4 UT on 28 September 2017. The white dashed line gives the cross section that is for producing the north-south keogram in Figure 5. (a) Red lines are PsA patches in the EMCCD ASI. (b) We reproduce the red outlines in (a) to better see the correspondence between the two data sets.

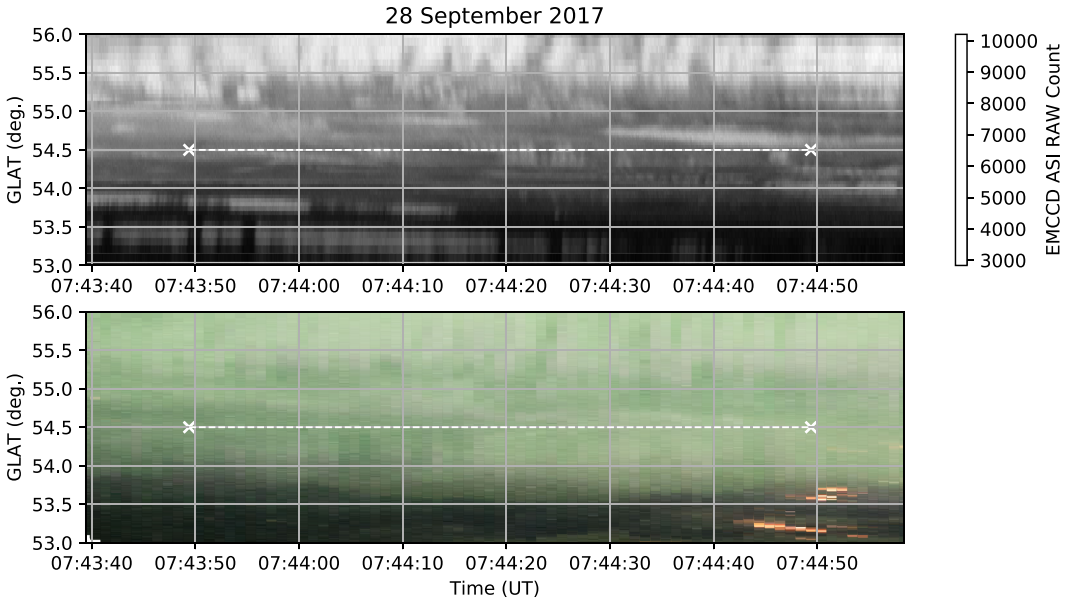

Figure 5. N-S keogram along the cross sections shown by the white dashed line in Figure 4. The top panel is from the EMCCD ASI, and the bottom panel is from the ISS camera. The white dashed line shows the interval used for the cross-correlation analysis shown in Figure 6.

camera systems. An animation showing the full sequence of this PsA interval accompanies the electronic version of this article (Supporting Information Movie S2). To map the EMCCD ASI data from Athabasca, we assumed the emission height of 100 km, and the data whose elevation angle is larger than 30° are plotted. The mapped EMCCD ASI image (black and white data in Figure 4a) shows that there were a few patches of PsA at this time, which were outlined by the red lines. These PsA patches are seen in the ISS image as white and/or pink regions in the northern half of the mapped area. It is a little hard to find one-to-one spatial correspondence between the location of PsA patches between the ISS and ASI images. For example, on the southeastern side of the FOV of the EMCCD ASI, the two arc-type PsAs were observed, but the ISS camera was not able to distinguish them. It is more difficult to find a good contrast between the bright (white and/or pink) and dark parts of the PsA patches in the ISS image than the EMCCD image. This could be due to the background continuous precipitation of PsA. Miyoshi et al. (2015) showed that, when PsA appears, there exist background continuous precipitations of low-energy (<1 keV) electrons even during the OFF phase (or outside PsA patches). While the EMCCD ASI observes prompt emission caused by high-energy (>1 keV) electrons, the ISS image contains contributions from both the low- and high-energy electrons. This might have made it difficult to identify the structure of PsA patches clearly.

Now we compare the temporal variation of the PsA observed by both the ISS camera and the EMCCD ASI. Figure 5 is the so-called keogram, made from the ASI and ISS images, which is a time series of the cross

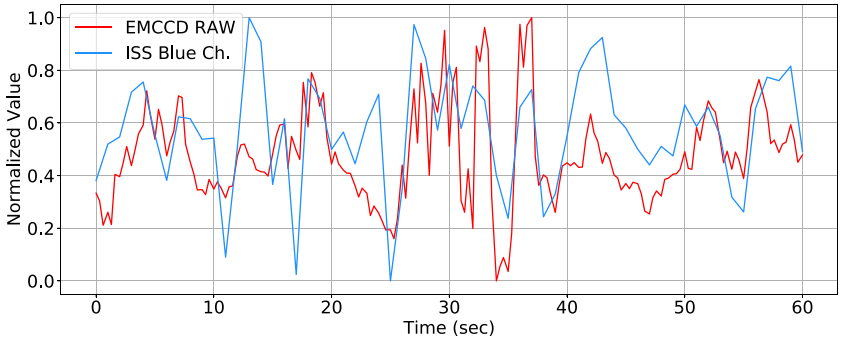

Figure 6. Time series of the optical intensity of PsA observed by the ISS camera and the EMCCD ASI. The vertical axis is the normalized ISS image blue channel (blue) and the ASI image raw count (red).

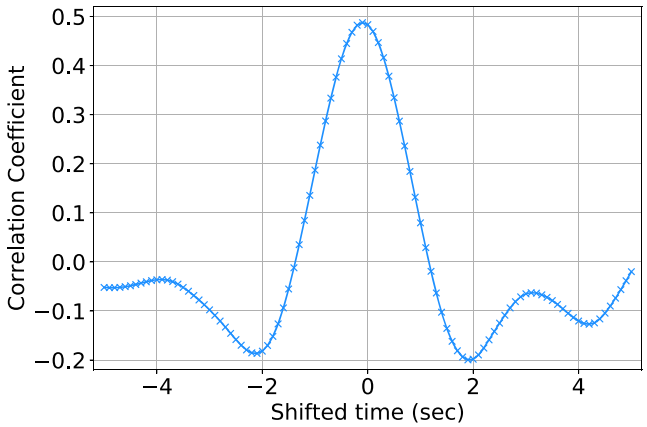

Figure 7. Cross-correlation coefficient between the two time series shown in Figure 6. The horizontal axis is the time lag between the two data sets.

sections depicted by the white dashed line in Figure 4. In both the data, clear signatures of optical pulsations are seen in the latitude range from 55° N to 56° N, which are manifestations of PsA in the keogram. The period of PsA ranges from 3 to 5 s in this interval, which is more clearly identified in the EMCCD ASI data. More importantly, optical pulsation is also seen in the ISS data, and the periodicity is likely to be the same.

To better see the correspondence between the two cameras, we plotted the data in the central 1 min interval indicated by the white dashed line as time series in Figure 6. Here, to remove the background trend, the moving average was subtracted, and the variations whose periodicity is longer than 10 s have been filtered out. In addition, we have normalized the values of the blue channel of the ISS images (blue) and the raw count value of the ASI images (red). Although the magnitudes of the two lines do not always agree with each other, there exist a peak-to-peak correspondence between the two variations. This implies that both the camera systems detected common temporal variations of PsA. In addition, we calculated the cross-correlation coefficient between the two time series by shifting time every 0.1 s, which is shown in Figure 7. The best correlation coefficient was 0.5 with a time lag of 0.1 s, which indicates that the error in the calibrated time of the ISS camera is less than at least 0.1 s.

4. Discussion and Conclusion

From the calibration results summarized in Table 1, it was implied that the imaging parameters were constant regardless of time. This indicates that it is sufficient to calibrate the imaging parameters once at one place in a single sequence. Therefore, if there is a single image including city lights without cloud contamination in the sequence, aurora could be mapped even if the rest area is covered by cloud. For the image sequence in the southern hemisphere, if the South Africa or the Australian is captured, the mapping of aurora is possible even over the sea.

For the case of discrete aurora, as shown in Figures 2c–2e, the aurora arcs extending in the north-south direction were observed in the same location by the two camera systems. The displacement was less than 0.1° (~5 km) in the longitudinal direction. Although there was a difference of 0.4 s in the timing of the image capturing of both the cameras, this result suggests that the accuracy of the mapping in the direction perpendicular to the line of sight of the ISS camera (i.e., E-W direction in this case) is less than 5 km, and possible error in the calibrated time of the ISS image is at least less than 3 s (the temporal resolution of the THEMIS ASI). In contrast, another discrete feature indicated by the blue line in Figure 3 was not observed in the same location by the two cameras. Although this difference might have been due to the contamination by clouds in the ground-based ASI image, it is more likely that the accuracy in the mapping of the ISS image depends on the viewing direction. That is, the mapping is inaccurate for structure perpendicular to the line of sight of the ISS camera. This should be taken into account when we examine the L-shell aligned discrete aurora because the line of sight of the ISS camera is perpendicular to the local L-shell in many cases.

For the case of PsA, the temporal variations of optical pulsation demonstrated in the keogram in Figure 5 were similar in both the cameras. That is, periodic enhancements in the luminosity are commonly identified in both the keograms. The results shown in Figures 6 and 7 suggest that the calibrated time is correct within 0.1 s. However, since the time lag parameter has a standard deviation of 0.3 s, as summarized in Table 1, we conclude that the temporal accuracy should be at least within 0.3 s. In addition, it was indicated that the spatial structure parallel to the line of sight of the ISS camera was not correctly mapped except in the lower altitude part of aurora because their height profiles should be projected on the plane as shown in Figure 4. Therefore, when analyzing the data set obtained by the proposed method, it is necessary to pay attention to the effect of the height profile of aurora on the mapped horizontal structure. The temporal variation is a manifestation of "main pulsation" of PsA, whose period ranges from a few to a few tens of second (e.g., Lessard, 2012; Yamamoto, 1988) shown in the upper part of both keograms. Since the temporal resolution of the ISS camera was 1 s for the current case, it is possible to track this main pulsation using the digital camera observations from ISS. The keogram made from the EMCCD ASI shows tiny scintillation in the optical

intensity embedded within single pulses of main pulsation, that is, the so-called 3 Hz internal modulation (e.g., Røyrvik & Davis, 1977). Important point is that similar quicker variation is not seen in the keogram of the ISS data, which indicates a limitation of the ISS camera to detect the internal modulation of PsA directly due to the insufficient temporal resolution of the image capturing.

The mapping method using star light positions proposed by Riechert et al. (2016) did not guarantee the time accuracy, but they argued that the time accuracy improved within 1 s or less by additional use of city light positions. However, since the window distortion was not taken into consideration, there were geographical errors of about 20 km even after using city light positions. In this research, we calibrated the time accuracy within an order of 0.1 s. Therefore, the proposed method has a certain advantage to the previous one especially when observing aurora that rapidly change their shape and luminosity like PsA. In particular, when observing a PsA whose spatial extent is ~30 km in the latitudinal direction shown in Ozaki et al. (2018), our method has a great advantage compared to that of Riechert et al. (2016).

Since the periodicity of the main pulsation of PsA ranges from a few to a few tens of second, the ISS images can be used to observe its modulation with sufficient temporal resolution. However, since the periodicity of the internal modulation of PsA is around several Hertz, thus, it is difficult to find its signature in the ISS images. Recently, several characteristics of PsA, such as their shape, periodicity, and temporal evolution, have been investigated. For example, the statistical analysis of the size of patchy pulsating aurora (PPA) was performed by Partamies et al. (2019). They suggested that the size of PPA increases during the substorm expansion phase. Although, in that study, they were able to track PPA from the beginning to the end of the entire interval using a ground-based ASI, it was difficult to visualize their large-scale spatial distribution at the same time under the same geomagnetic condition. In contrast to such a study using ground-based ASIs, the ISS images cannot be used to observe the same area for a long time, but it could be used to track the spatiotemporal evolution of aurora, including PsA, in a wide area for a short interval (~10 min) because the FOV of the camera sweeps the surface of the Earth along the trajectory of ISS.

Yang et al. (2015) demonstrated that PPA moves with the background plasma convection by comparing the ionospheric drift from SuperDARN (Super Dual Auroral Radar Network) with the speed of PPA estimated by the ground-based optical data. This indicates that the motion of PPA is controlled by the $E \times B$ drift at the ionospheric altitudes, suggesting that the motion and spatial structure of PsA are closely related to those of cold plasma in the source region near the equatorial plane of the magnetosphere. Utilizing the current data sets having wide FOV will enable us to reveal the relationship between the larger-scale plasma convection and the motion of PPA in detail. In addition, the ISS images have three color channels, that is, red, green, and blue channels. Given that the green channel corresponds to the 5,577 Å emission of O and the blue corresponds to the band emission of N_2^+, it might be possible to estimate the energy of the aurora from the ratio between RGB values. Hosokawa and Ogawa (2015) suggested that the energy of PsA electrons tends to be higher in the morning side rather than the night side. Such a tendency could also be confirmed by using the ISS images covering a wide area in the direction of the magnetic local time.

5. Summary

We introduced a method for mapping the full-color photographs of aurora that have been taken with digital single-lens reflex cameras mounted on the ISS. The imaging parameters of these images were estimated by the calibration method using city lights proposed by Hozumi et al. (2016), and these images were projected to the altitude of auroral emission. Comparison with simultaneous optical observations from the ground suggests that the time accuracy of the current estimation is less than 0.3 s and the spatial accuracy is less than 5 km in the direction perpendicular to the looking direction of the camera. In the direction parallel to the line of sight, however, mapping is less accurate because the vertical structure of aurora is mapped onto the horizontal plane. We also succeeded in extracting temporal variations of PsA, ranging from a few to a few tens of second, from the ISS images. The cameras used for this observation have a wide FOV (~1,100 × 900 km) and sweep the aurora oval in the longitude direction in a short time (~10 min), which enables us to visualize the large-scale (>1,000 km) structure of aurora in a fine-scale (<30 km). Such completely new imaging data from space are particularly useful for analyzing the spatiotemporal characteristics of PsA, which can contribute to better understanding the generation and loss processes of space plasma by using aurora as a tracer.

Acknowledgments
This work was supported by Grants-in-Aid for Scientific Research (15H05747, 15H05815, 16H06286, 17H00728, and 18KK0100) from the Japan Society for the Promotion of Science. The auroral photographs taken from ISS are courtesy of the Earth Science and Remote Sensing Unit, NASA Johnson Space Center. The photographs taken from ISS are available online (https://eol.jsc.nasa.gov/). We thank NOAA's National Geophysical Data Center and U.S. Air Force Weather Agency for the provision of the global nighttime stable light data obtained from the visible and infrared sensors (OLS) on the Defense Meteorological Satellite Program (DMSP) satellite. The city light images taken by OLS are available online (https://ngdc.noaa.gov/eog/dmsp/downloadV4composites.html). The authors acknowledge NASA Contract NAS5-02099 for the use of data from the THEMIS Mission. Specifically, we thank S. Mende and E. Donovan for use of THEMIS ASI data. The ASI data are available online (http://themis.ssl.berkeley.edu/index.shtml). The EMCCD ASI data taken at Athabasca are available at the ERG Science Center operated by ISAS/JAXA and ISEE/Nagoya University (https://ergsc.isee.nagoya-u.ac.jp/psa-pwing/pub/dset/20170928&urluscore;ath/).

References

Acuña, M. H., Ogilvie, K. W., Baker, D. N., Curtis, S. A., Fairfield, D. H., & Mish, W. H. (1995). The Global Geospace Science Program and its investigations. *Space Science Reviews*, *71*(1), 5–21. https://doi.org/10.1007/BF00751323

Akasofu, S.-I. (1965). Dynamic morphology of auroras. *Space Science Reviews*, *4*(4), 498–540. https://doi.org/10.1007/BF00177092

Asamura, K., Chaston, C., Itoh, Y., Fujimoto, M, Sakanoi, T., Ebihara, Y., et al. (2009). Sheared flows and small-scale Alfvén wave generation in the auroral acceleration region. *Geophysical Research Letters*, *36*, L05105. https://doi.org/10.1029/2008GL036803

Brown, D. C. (1971). Close-range camera calibration. *Photogrammetric Engineering*, *37*(8), 855–866.

Brown, N. B., Davis, T. N., Hallinan, T. J., & Stenbaek-Nielsen, H. C. (1976). Altitude of pulsating aurora determined by a new instrumental technique. *Geophysical Research Letters*, *3*(7), 403–404. https://doi.org/10.1029/GL003i007p00403

Burch, J. L. (2000). IMAGE mission overview. In J. L. Burch (Ed.), *The IMAGE mission* (pp. 1–14). Dordrecht: Springer Netherlands. https://doi.org/10.1007/978-94-011-4233-5&urluscore;1

Burch, J. L., Mende, S. B., Mitchell, D. G., Moore, T. E., Pollock, C. J., Reinisch, B. W., et al. (2001). Views of Earth's magnetosphere with the IMAGE satellite. *Science*, *291*(5504), 619–624. https://doi.org/10.1126/science.291.5504.619

Davis, T. N. (1966). The application of image orthicon techniques to auroral observation. *Space Science Reviews*, *6*(2), 222–247. https://doi.org/10.1007/BF00222594

Elphinstone, R. D., Hearn, D. J., Cogger, L. L., Murphree, J. S., Singer, H., Sergeev, V., et al. (1995). Observations in the vicinity of substorm onset: Implications for the substorm process. *Journal of Geophysical Research*, *100*(A5), 7937–7969. https://doi.org/10.1029/94JA02938

Gateway to Astronaut Photography of Earth (1995). https://eol.jsc.nasa.gov/.(Accessed 13 Oct 2019)

Hosokawa, K., Miyoshi, Y., & Li, W. (2015). Introduction to special section on pulsating aurora and related magnetospheric phenomena. *Journal of Geophysical Research: Space Physics*, *120*, 5341–5343. https://doi.org/10.1002/2015JA021453

Hosokawa, K., & Ogawa, Y. (2015). Ionospheric variation during pulsating aurora. *Journal of Geophysical Research: Space Physics*, *120*, 5943–5957. https://doi.org/10.1002/2015JA021401

Hozumi, Y., Saito, A., & Ejiri, M. K. (2016). Calibration of imaging parameters for space-borne airglow photography using city light positions. *Earth, Planets and Space*, *68*(1), 155. https://doi.org/10.1186/s40623-016-0532-z

Jähne, B. (1997). *Practical handbook on image processing for scientific and technical applications*. Boca Raton: CRC Press Inc.

Jones, A. V. (1971). Auroral spectroscopy. *Space Science Reviews*, *11*(6), 776–826.

Kataoka, R., Miyoshi, Y., Shigematsu, K., Hampton, D., Mori, Y., Kubo, T., et al. (2013). Stereoscopic determination of all-sky altitude map of aurora using two ground-based Nikon DSLR cameras. *Annales Geophysicae*, *31*(9), 1543–1548. https://doi.org/10.5194/angeo-31-1543-2013

Killeen, T. L., Craven, J. D., Frank, L. A., Ponthieu, J.-J., Spencer, N. W., Heelis, R. A., et al. (1988). On the relationship between dynamics of the polar thermosphere and morphology of the aurora: Global-scale observations from Dynamics Explorers 1 and 2. *Journal of Geophysical Research*, *93*(A4), 2675–2692. https://doi.org/10.1029/JA093iA04p02675

Lessard, M. R. (2012). A review of pulsating aurora. In *Auroral phenomenology and magnetospheric processes: Earth and other planets* (pp. 55–68). Washington, DC: American Geophysical Union. https://doi.org/10.1029/2011GM001187

Marklund, G. T., Karlsson, T., Blomberg, L. G., Lindqvist, P.-A., Fälthammar, C.-G., Johnson, M. L., et al. (1998). Observations of the electric field fine structure associated with the westward traveling surge and large-scale auroral spirals. *Journal of Geophysical Research*, *103*(A3), 4125–4144. https://doi.org/10.1029/97JA00558

Mende, S. B., Harris, S. E., Frey, H. U., Angelopoulos, V., Russell, C. T., Donovan, E., et al. (2008). The themis array of ground-based observatories for the study of auroral substorms. *Space Science Reviews*, *141*(1-4), 357. https://doi.org/10.1007/s11214-008-9380-x

Mende, S. B., Heetderks, H., Frey, H. U., Lampton, M., Geller, S. P., Abiad, R., et al. (2000). Far ultraviolet imaging from the IMAGE spacecraft. 2. Wideband FUV imaging. *Space Science Reviews*, *91*(1), 271–285. https://doi.org/10.1023/A:1005227915363

Milan, S. E., Hutchinson, J., Boakes, P. D., & Hubert, B. (2009). Influences on the radius of the auroral oval. *Annales Geophysicae*, *27*(7), 2913–2924. https://doi.org/10.5194/angeo-27-2913-2009

Miyoshi, Y., Saito, S., Seki, K., Nishiyama, T., Kataoka, R., Asamura, K., et al. (2015). Relation between fine structure of energy spectra for pulsating aurora electrons and frequency spectra of whistler mode chorus waves. *Journal of Geophysical Research: Space Physics*, *120*, 7728–7736. https://doi.org/10.1002/2015JA021562

Nishiyama, T., Sakanoi, T., Miyoshi, Y., Kataoka, R., Hampton, D., Katoh, Y., et al. (2012). Fine scale structures of pulsating auroras in the early recovery phase of substorm using ground-based EMCCD camera. *Journal of Geophysical Research*, *117*, A10229. https://doi.org/10.1029/2012JA017921

Oguti, T., Kaneda, E., Ejiri, M., Sasaki, S., Kadokura, A., Yamamoto, T., et al. (1990). Studies of aurora dynamics by Aurora-TV on the Akebono (EXOS-D) satellite. *Journal of Geomagnetism and Geoelectricity*, *42*(4), 555–564. https://doi.org/10.5636/jgg.42.555

Ozaki, M., Shiokawa, K., Miyoshi, Y., Hosokawa, K., Oyama, S., Yagitani, S., et al. (2018). Microscopic observations of pulsating aurora associated with chorus element structures: Coordinated Arase satellite-PWING observations. *Geophysical Research Letters*, *45*, 12,125–12,134. https://doi.org/10.1029/2018GL079812

Ozaki, M., Shiokawa, K., Miyoshi, Y., Kataoka, R., Yagitani, S., Inoue, T., et al. (2016). Fast modulations of pulsating proton aurora related to subpacket structures of Pc1 geomagnetic pulsations at subauroral latitudes. *Geophysical Research Letters*, *43*, 7859–7866. https://doi.org/10.1002/2016GL070008

Partamies, N., Bolmgren, K., Heino, E., Ivchenko, N., Borovsky, J. E., & Sundberg, H. (2019). Patch size evolution during pulsating aurora, pp. 4725–4738. https://doi.org/10.1029/2018JA026423

Riechert, M., Walsh, A. P., Gerst, A., & Taylor, M. G. G. T. (2016). Automatic georeferencing of astronaut auroral photography. *Geoscientific Instrumentation, Methods and Data Systems*, *5*(2), 289–304. https://doi.org/10.5194/gi-5-289-2016

Romick, G. J., & Belon, A. E. (1967). The spatial variation of auroral luminosity—I: The behavior of synthetic model auroras. *Planetary and Space Science*, *15*(3), 475–493. https://doi.org/10.1016/0032-0633(67)90157-2

Røyrvik, O., & Davis, T. N. (1977). Pulsating aurora: Local and global morphology. *Journal of Geophysical Research*, *82*(29), 4720–4740. https://doi.org/10.1029/JA082i029p04720

Sakanoi, T., Okano, S., Obuchi, Y., Kobayashi, T., Ejiri, M., Asamura, K., & Hirahara, M. (2003). Development of the multi-spectral auroral camera onboard the INDEX satellite. *Advances in Space Research*, *32*(3), 379–384. https://doi.org/10.1016/S0273-1177(03)90276-6

Samara, M., Michell, R., & Hampton, D. (2012). BG3 glass filter effects on quantifying rapidly pulsating auroral structures. *Advances in Remote Sensing*, *1*, 53–57. https://doi.org/10.4236/ars.2012.13005

Scourfield, M. W. J., & Parsons, N. R. (1969). An image intensifier-vidicon system for auroral cinematography. *Planetary and Space Science*, *17*(1), 75–81. https://doi.org/10.1016/0032-0633(69)90124-X

Trucco, E., & Verri, A. (1998). *Introductory techniques for 3-D computer vision*. Englewood Cliffs, NJ: Prentice Hall.

Version 4 DMSP-OLS Nighttime Lights Time Series (2015). https://ngdc.noaa.gov/eog/dmsp/downloadV4composites.html. (Accessed 13 Oct 2019).

Yamamoto, T. (1988). On the temporal fluctuations of pulsating auroral luminosity. *Journal of Geophysical Research*, *93*(A2), 897–911. https://doi.org/10.1029/JA093iA02p00897

Yang, B., Donovan, E., Liang, J., Ruohoniemi, J. M., & Spanswick, E. (2015). Using patchy pulsating aurora to remote sense magnetospheric convection. *Geophysical Research Letters*, *42*, 5083–5089. https://doi.org/10.1002/2015GL064700

Zhang, Y., Paxton, L. J., Immel, T. J., Frey, H. U., & Mende, S. B. (2002). Sudden solar wind dynamic pressure enhancements and dayside detached auroras: IMAGE and DMSP observations. *Journal of Geophysical Research*, *107*(A4), COA 2–1–COA 2–11. https://doi.org/10.1029/2002JA009355